Engineering Fracture Mechanics 264 (2022) 108355

Contents lists available at ScienceDirect

Engineering Fracture Mechanics

journal homepage: www.elsevier.com/locate/engfracmech

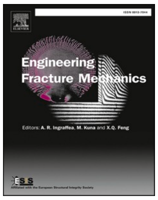

Effect of surface finish metallization layer on shearing fracture toughness of sintered silver bonded joints

Shuai Zhao [a], Yanwei Dai [a,b,*], Fei Qin [a,b,*], Yanning Li [a], Tong An [a,b], Yanpeng Gong [a,b]

[a] *Institute of Electronics Packaging Technology and Reliability, Faculty of Materials and Manufacturing, Beijing University of Technology, Beijing 100124, China*
[b] *Beijing Key Laboratory of Advanced Manufacturing Technology, Faculty of Materials and Manufacturing, Beijing University of Technology, Beijing 100124, China*

ARTICLE INFO

Keywords:
Sintered Ag
Shearing fracture toughness
Metallization layers
Microstructure
Interface property

ABSTRACT

In this paper, the effect of different surface finish metallization layers (Cu, Ni, Au and Ag) on the shearing fracture toughness of sintered Ag bonded joints under various sintering temperatures is investigated based on end-notch flexure (ENF) test. The results show that the shearing fracture toughness for different kinds of specimens all increase with the sintering temperature augment. The sintered Ag/Ag joint shows the highest shearing fracture toughness while the sintered Ag/Ni joint shows the lowest. The average shearing fracture toughness of the Ag/Cu joint is very close to the Ag/Au joint when sintered from 240 °C to 280 °C, whereas the former became much higher when sintered under 300 °C. By statistically analysis of crack propagation paths, interface microstructure characteristics, and interface reaction, it is found that the main factors affecting the discrepancy of the shearing fracture toughness for different metallized layers are the interface connection ratio and contact angle. A higher interface connection ratio and lower contact angle can increase the actual crack resistance and lower down stress concentration at the bonding interface, which leads to the discrepancy of shearing fracture toughness correspondingly. The different inter-diffusion rates for Ag and various metallization layers are also clarified. This study could deepen the understanding of the metallization layer effect on the shearing fracture behaviors of sintered silver bonded joints.

1. Introduction

Sintered silver (Ag) is regarded as the most promising die-attach material for the packaging of the next generation power electronics, especially silicon carbide (SiC) power electronics, due to its excellent thermal and electrical properties [1]. Compared with traditional lead-free solder joints, sintered Ag possesses a high melting temperature (960 °C) and outstanding thermal (240 $\mathrm{W{\bullet}m^{-1}{\bullet}k^{-1}}$) and electrical conductivity (4.1×10^7 $\mathrm{S{\bullet}m^{-1}}$) [2]. All these attractive features make the power modules possibly long-

---

Abbreviations: Ag, silver; ENIG, electroless Nickel/immersion Gold; AgNPs, silver nanoparticles; Cu, copper; CBBM, Compliance Based Beam Method; ENF, End-Notch-Flexure.

[*] Corresponding authors at: Institute of Electronics Packaging Technology and Reliability, Faculty of Materials and Manufacturing, Beijing University of Technology, Beijing 100124, China.

E-mail addresses: ywdai@bjut.edu.cn (Y. Dai), qfei@bjut.edu.cn (F. Qin).

https://doi.org/10.1016/j.engfracmech.2022.108355
Received 16 December 2021; Received in revised form 21 February 2022; Accepted 22 February 2022

terms operating at a high temperature environment over 250 °C [3]. In addition, the micro-sized or nano-sized Ag pastes can be sintered at a relative low temperature (<300 °C) in low pressure (<5 MPa) or even pressureless condition, which is benefit for wide industrial applications [4]. Hence, the sintering technologies of different kinds of Ag pastes have attracted tremendous attentions in recent years [5–6].

As sintered Ag is the key channel for electrical transport and heat dissipation between the SiC die and direct bonding copper (DBC) substrate, the bonding performance is crucial to determine the quality of sintering processes and mechanical reliability. Some investigations have shown that sintering parameters play an important role on the bonding strength of sintered Ag, e.g., sintering pressure, heating rate, sintering temperature, holding time, and sintering atmosphere [7–8]. More recently, the bonding quality of sintered Ag on the surface of copper (Cu) substrate has received some attentions, as it has been proved that the interface between the sintered Ag and Cu substrate is more prone to failure during the long-term operation environment [9–10]. As the upper surface of the Cu substrate is usually plated with different metallization layers for oxidation or corrosion prevention [11–12], it is of great significance to study the effect of the metallization layers on the bonding performance of sintered Ag joint.

Traditional method to assess the bonding performance of sintered Ag joint is based on die-shearing test, in which the critical shearing strength is defined as the ratio of the maximum shearing force to the bonding area. Lee et al. [13] and Yoon et al. [14] studied the effect of three different surface finishing metallization of Cu, Ag and electroless Nickel/immersion Gold (ENIG) on the shearing strength of sintered Ag joint. It is found that the Ag/Ag sintered joint shows a superior shearing strength than the Ag/Au and Ag/Cu sintered joint, and the Ag/Cu sintered joint shows the lowest. Similar results were also reported by Chen et al. [15–16]. Xu et al. [17] and Fan et al. [18] investigated the shearing strength of sintered Ag on Au surface finishing substrate metallized by electroplated Ni/Au and ENIG, and the results show that the former value is much higher. Wang et al. [19–20] investigated pressureless Ag sintering on Ni-plated substrates, they found that the shearing strength can reach to 40 MPa by choosing proper Ag materials and sintering temperature. Du et al. [21–22] investigated the bonding performance of sintered Ag on bare copper substrates, and the results show that a high shearing strength of 40 MPa can also be obtained by using Cu substrates with smaller grain sizes. In contrast, Zhang et al. [23] found the bonding strength of sintered Ag joining on Au surface finished substrate was enhanced by increasing Au grain size. Recently, Chen et al. [24] studied four different kinds of Au plating processes on the shearing strength of sintered Ag-Au joints, the results show that the bonding strength are strongly related to the grain orientation of the plated Au layers.

Those investigations reviewed above all evaluate the bonding quality of sintered Ag on different metallized substrates based on die-shearing tests. Although die-shearing test is a very convenient and widely used method in engineering application, it is not sufficient to characterize the bonding performance of sintered Ag joints. As is known, the as-sintered Ag layer is more prone to exhibit a brittle feature due to its porous structure, such property makes it cracking easily under harsh thermal-mechanical stresses [25–26]. Thus, the fracture toughness of the sintered Ag joint is also an important index to assess its bonding performance and fracture behavior. Wang et al. [27] investigated the mode I (opening-mode) fracture toughness (K_{IC}) of sintered Ag on both bare Cu and Ni/Au-plated substrate based on the modified compact tension test. It is found that both the K_{IC} of Au/AgNPs (silver nanoparticles) and Cu/AgNPs are strongly related to the sintering temperature, and the former is a little bit higher in most conditions. Recently, Qin et al. [28] reported the effect of metallization layer on the interfacial cracking behaviors using numerical analysis, the results show that the interfacial cracking of sintered Ag and Cu substrate in a SiC power module under thermal-mechanical stress are much close to a shearing mode. Hence, it is also very significant to verify the effect of different metallization layers on the shearing fracture toughness of sintered Ag joints.

Several methods haven been developed by researchers to determine mode II fracture toughness of adhesive materials, e.g., End-Notch-Flexure (ENF) [29–30], end-loaded Spilt (ELS) [31] and Four-Point End-Notch Flexure (4ENF) tests [32], in which the ENF test is generally regarded as the most suitable method to estimate the shearing fracture toughness of bonded joints due to its simplicity and accurate data reduction methods [33–34]. In our previous work [35–36], ENF test was adopted and proved robustly to assess the shearing fracture toughness of sintered Ag on bare Cu substrate. In this paper, the effect of different surface finish metallization layers, e.g., Cu, Ni, Au and Ag on the shearing fracture behaviors of sintered Ag joints under different sintering temperatures were studied. Toward this aim, series of ENF tests are executed with the Cu substrates of the specimens plated by different metallization layers. The fracture types, microstructure and interfacial reactions are analyzed to reveal the possible bonding and fracture mechanism of sintered Ag joints with different metallization layers. Explanations and comparisons of different surface finish metallization layers on shearing fracture behaviors for sintered silver bonding joints are also presented.

The organization of this paper is as following. The experimental procedures of the ENF test and microstructure characterization method are presented in Section 2. The results of the ENF tests, shearing fracture behaviors, and microstructure of the sintered Ag bonded joints with different metallization layers are given in Section 3. In Section 4, the interfacial reactions are analyzed to discuss the possible influence mechanism of the metallization layer on the shearing fracture toughness of the sintered Ag joint. The conclusions are summarized in the last section.

2. Experimental procedures

2.1. Sample preparation and ENF test

The Ag paste used in this paper is a kind of hybrid Ag paste (Henkel Corporation, LOCTITE ABLESTIK SSP 2020), which is mixed with micron-sized Ag flakes and submicron-sized Ag particles. The specimen is composed of two Cu substrates and a sintered Ag layer. Before the specimens were fabricated, the surfaces of the Cu substrates were ground by 400#, 800#, 2000# SiC abrasive papers in turn and then polished with 1 μm diamond grinding fluid. For the samples with metallization layers, similar as-polished Cu substrates were further electroplated with Ni, Ni/Au and Ni/Ag layers. The thicknesses of the Ni, Ni/Au and Ni/Ag layers are 2 μm, 2/0.16 μm and 2/

0.16 μm, respectively. Fig. 1(a) shows the schematic view and design dimensions of the ENF specimen. The detail fabrication processes of the specimens can refer to our previous work [35], which is described briefly here. First, all the substrates after metallization were ultrasonically cleaned in acetone and ethanol in turn each for 15 min. After that, the Ag pastes were screen-printed on one Cu substrate with a thickness of 100 μm and then bonded with the other substrate together using a jig. All the specimens with different metallization layers after bonding were pressure-less sintered in a reflow oven with different sintering parameters. As shown in Fig. 1(b), the ENF specimens were firstly heated to 240 °C, 260 °C, 280 °C and 300 °C, respectively, with a heating rate of 10 °C/min, then sintered isothermally for 60 min. After that, the specimens were naturally cooled down to ambient temperature.

All the as-sintered specimens were tested on a three-point bending fixture using Instron 5948, as shown in Fig. 1(c). The half-span length and initial crack length were set as 40 mm and 20 mm, respectively. During the testing process, the specimen was supported by the three-point bending fixture and the loading head was moving down with a rate of 0.2 mm/min. The curves of the load P respect to the displacement δ (P-δ curves) were recorded timely by the sampling system of the Instron 5948. For each condition, at least five specimens were tested.

The shearing fracture toughness G_{IIC} were calculated based on the Compliance Based Beam Method (CBBM), which has been proved accurate and efficient in data reduction for the ENF test [37–40]. According to the Timoshenko beam theory, the compliance of the ENF specimen C can be described as

$$C = \frac{3a_e^3 + 2L^3}{8E_f bh^3} + \frac{3L}{10Gbh^3} \tag{1}$$

where a_e is the equivalent crack length, L is the half-span length, b is the thickness of the adherend, E_f and G are the flexural and shear modulus of the adherend, respectively. According to Eq. (1), the flexural modulus of the specimen can be calculated using the initial compliance C_0 and the initial crack length a_0

$$E_f = \frac{3a_0^3 + 2L^3}{8bh^3 C_{0c}} \tag{2}$$

where C_{0c} is the corrected initial compliance which is given by

$$C_{0c} = C_0 - \frac{3L}{10Gbh} \tag{3}$$

Substituting Eq. (2) and Eq. (3) into Eq. (1), the equivalent crack length a_e can be written as

$$a_e = \left[\frac{C_c}{C_{0c}} a_0^3 + \frac{2}{3}\left(\frac{C_c}{C_{0c}} - 1\right) L^3\right]^{1/3} \tag{4}$$

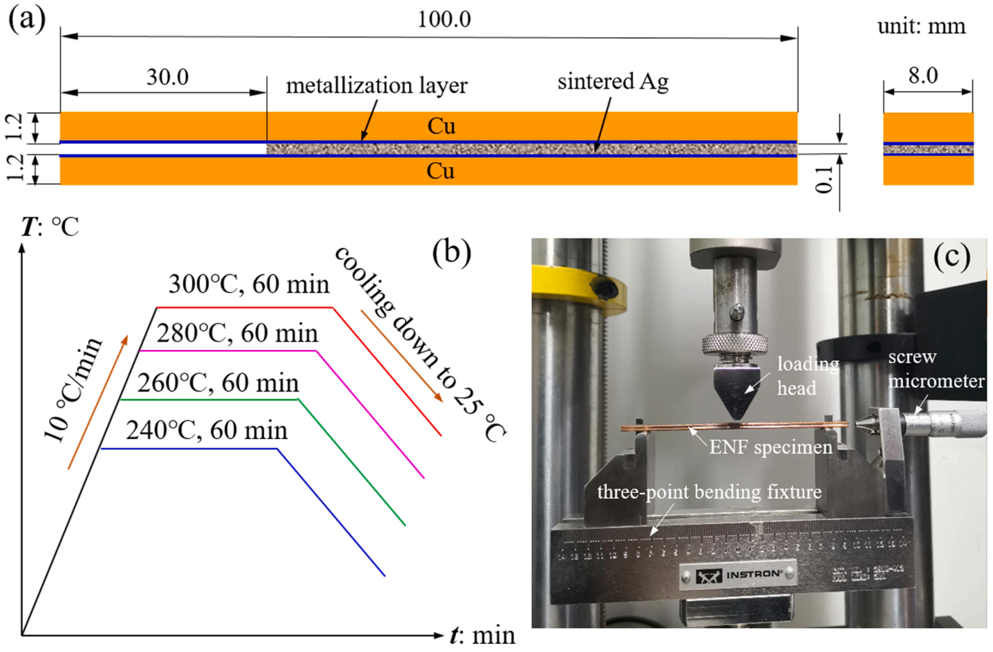

Fig. 1. ENF tests for the shearing fracture toughness measurement of sintered Ag joint with different metallized Cu substrates. (a) The schematic view and dimensions of the ENF specimen; (b) Four different sintering curves for the ENF specimens; (c) the ENF test using Instron 5948.

where C_c is the corrected compliance which can be obtained by Eq. (3) using C instead of C_0. According to Irwin-Kies equation, the shearing fracture toughness is given as:

$$G_{\mathrm{IIC}} = \frac{P^2}{2b}\frac{dC}{da} \tag{5}$$

Substituting Eq. (1), (2), (3) and (4) into Eq. (5) will lead to

$$G_{\mathrm{IIC}} = \frac{9P^2C_{0c}}{2b\left(3a_0^3+2L^3\right)}\left[\frac{C_c}{C_{0c}}a_0^3+\left(\frac{C_c}{C_{0c}}-1\right)\frac{2L^3}{3}\right]^{2/3} \tag{6}$$

It is seen that the calculation of G_{IIC} only requires the compliances and shear modulus, without additional crack length measurement during the crack propagation. Moreover, a typical value of G can be used in the G_{IIC} calculation, due the fluctuation of shear modulus has little effect on the calculation results [41].

2.2. Microstructure characterization

All the tested specimens were cold mounted by epoxy resign and the cross-sections were prepared using a metallographic sample polishing machine (MPD-2W). Then the fracture morphology of the tested specimens and the microstructure of the sintered Ag joint were observed by a field emission scanning electron microscope (FE-SEM, FEI Quanta 650). To explain the difference of the shearing fracture toughness of the sintered Ag joints in each sintering condition, the “apparent” porosity and Ag particle size were quantitatively analyzed using ImageJ software. The “apparent” porosity and particle size are defined as the proportion of pores and the average diameter of the Ag particles in a two-dimensional (2D) cross-section image, respectively. The interface connection ratio of the sintered Ag joints was also analyzed by calculating the connection length of the sintered Ag with the metallization layer in a selected interface length. Fig. 2 shows the schematic view of the measurement method of microstructure using ImageJ. The “apparent” porosity, Ag particle size and interface connection ratio can be calculated by the following equations:

$$\text{Porosity} = \frac{A_{pore}}{A_{total}} \times 100\% \tag{7}$$

$$\text{Particle size} = \frac{2\cdot\sum_{i=1}^{n}\left(\frac{A_i}{\pi}\right)^{1/2}}{n} \tag{8}$$

$$\text{Interface connection ratio} = \frac{\sum_{i=1}^{m}L_i}{L_{total}} \times 100\backslash\% \tag{9}$$

where A_{pore} is pore’s area, A_{total} is the total calculated area, A_i is the Ag particle’s area, n is the numbers of Ag particles, L_i is the

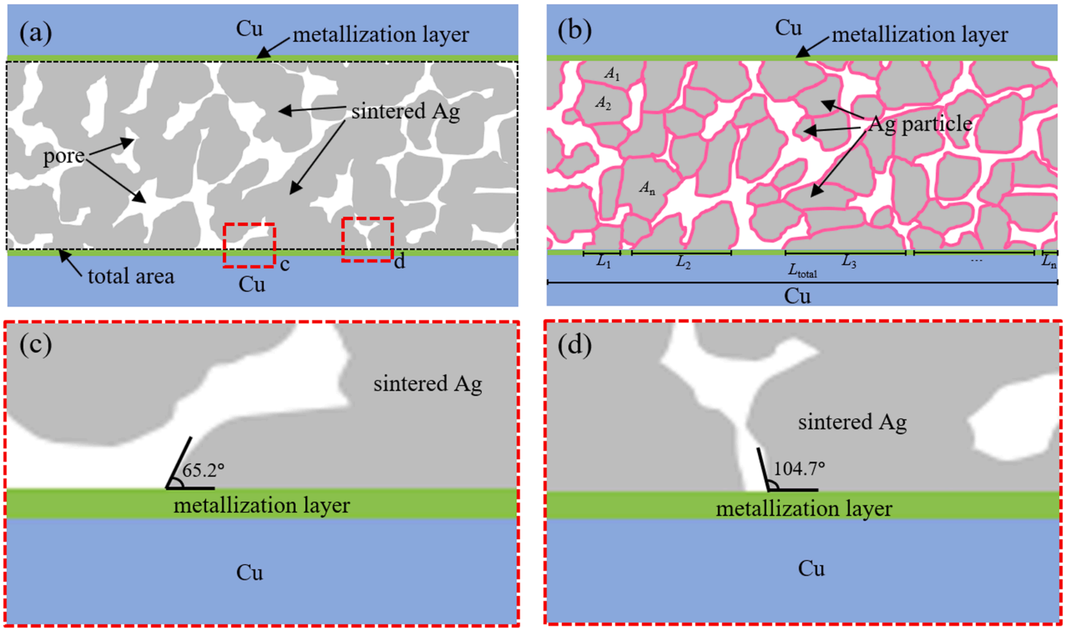

Fig. 2. The measurement of microstructure of the sintered Ag joints using ImageJ software. (a) porosity; (b) Ag particle size and interface connection ratio; (c) typical acute contact angle; (d) typical obtuse contact angle.

connection length, m is the numbers of the connection parts, and L_{total} is the total interface length. The interface contact angle between the Ag particle and the metallization layer were also summarized in Fig. 2. Fig. 2(c) and Fig. 2 (d) show the typical contact angle with an acute and obtuse angle, respectively. For each condition, five SEM images taken uniformly from the bonding lines were selected for the calculation. More details about the methods can refer to Refs. [42–44]. In addition, the element analysis and interface reaction of sintered Ag with different metallization layers were determined with an energy dispersive spectrometer (EDS) attached to FEI Quanta 650 SEM.

3. Results

3.1. Shearing fracture behaviors of sintered Ag joint with bare Cu, Ni, Ni/Au and Ni/Au metallized substrates

3.1.1. P-δ curves and shearing fracture toughness

In Fig. 3 (a)-(d) show the *P*-*δ* curves of the tested ENF specimens with bare Cu, plated Ni, plated Ni/Au, and plated Ni/Ag substrates, respectively. For most of the *P*-*δ* curves, the load value increases linearly with the proceed of the loading process, then a sudden drop appears and the crack starts to propagate once the load reach to the critical value. It indicates that the fracture of sintered Ag joints is consistent with the fracture of brittle materials [45]. For each type of specimen, the critical loads all increase with the increase of sintering temperature, which indicates that the critical fracture toughness exhibits a strengthen tendency with the increase of the sintering temperature. However, the critical values are quite different for the specimens with different surface finish metallization layers even sintered under the same temperatures. For the Ni-plated specimens, the critical loads are at a lowest level compared with the other specimens. The Ni/Ag plated specimens perform the highest critical load values. Especially, for the Ni/Ag plated specimens sintered under 300 °C, most of the specimens are not cracked even when large plastic deformation has occurred.

Fig. 4 shows the typical resistance curves (*R*-curves) calculated according to Eq. (4) and Eq. (6) for the different metallized specimens under various sintering temperatures, in which C1, C2, C3, C4 represent the conditions sintered under 240 °C, 260 °C, 280

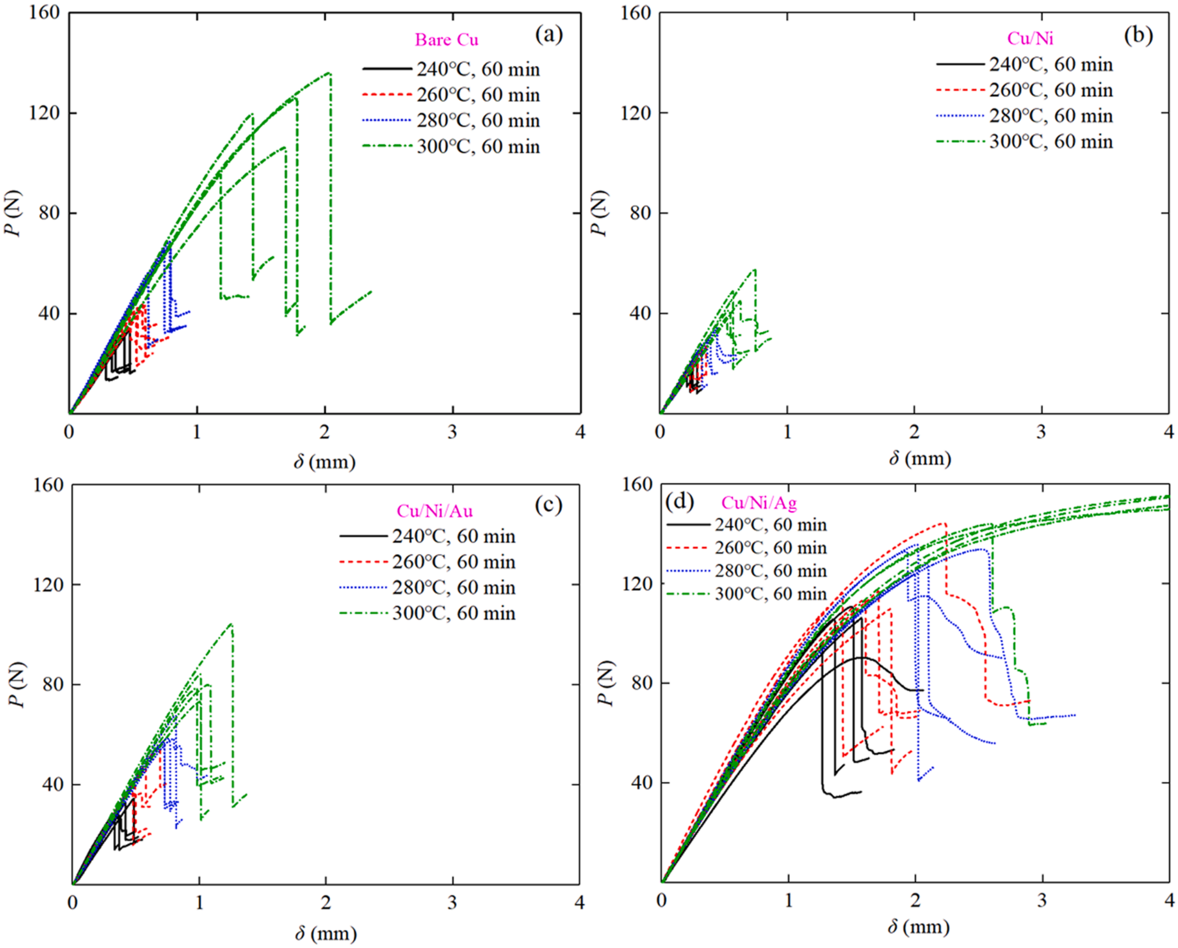

Fig. 3. *P*-*δ* curves of the ENF specimens with different metallization layers sintered under different temperatures (a) bare Cu; (b) plated Ni; (c) plated Ni/Au; (d) plated Ni/Ag.

°C and 300 °C, respectively. It is seen that the *R*-curve in each condition exists a plateau zone which indicates that a relatively steady G_{IIC} values are obtained during the crack propagation process. The tested G_{IIC} for each sintering condition is determined by averaging all the G_{IIC} values of the *R*-curves in the same condition.

Fig. 5 shows the computed average G_{IIC} of the sintered Ag joint on the Cu substrates with different metallization layers sintered under various temperatures. For each type of ENF specimen, the G_{IIC} heightens with the increase of sintering temperature. The Ni-plated specimens show the lowest average G_{IIC} value, which is only 50.28 $N{\bullet}m^{-1}$ even sintered under 300 °C. When sintered from 240 °C to 280 °C, the average G_{IIC} values of the sintered Ag joints on bare Cu substrates and Ni/Au-plated substrates are almost the same. However, the value of the bare Cu based ENF specimen is much higher than that of Ni/Au-plated specimen when sintered under 300 °C. For all the four types of ENF specimens, the Ni/Ag-plated specimens show the highest average G_{IIC} values. Even when sintered under 240 °C, the average G_{IIC} value is as high as 277.37 $N{\bullet}m^{-1}$. It should be mentioned that the toughness of the Ni/Ag-plated specimens is tough enough when sintered under 300 °C that most of the specimens don't show clear crack propagation processes. The minimum average values can sustain the whole loading process is 969.42 $N{\bullet}m^{-1}$, which can be calculated based on the numerical method we have reported in Ref. [35].

3.1.2. *Shearing fracture morphologies*

Figs. 6-9 show the typical shearing fracture morphologies of the ENF specimens with bare Cu, Ni-plated, Ni/Au-plated and Ni/Ag plated substrates sintered under various temperatures, respectively. The results show that the typical crack propagation paths for each kind of specimen are with obvious discrepancy. For the specimens with bare Cu substrates, the typical cracks all propagate along the interface of the sintered Ag and Cu substrates when sintered from 240 °C to 280 °C. Then the crack turns to propagate in the interior of the sintered Ag layer if the sintering temperature raises to 300 °C. However, for the specimens with Ni-plated and Ni/Au-plated layers, the cracks all propagate along the interface between the sintered Ag and the plated layer when sintered from 240 °C to 300 °C. For the specimens with Ni/Ag-plated layers, when sintered under 240 °C, the typical crack propagates along the interface between the sintered Ag and plated Ag layer. However, the cracks turn to propagate in the interior of sintered Ag layer when sintered from 240 °C to 280 °C. When sintered under 300 °C, the sintered Ag joints are tough enough that even a micro-crack exists at the edge of the sintered Ag layer, the crack doesn't propagate along the sintered Ag bonding line.

3.2. *Microstructure of sintered Ag joint on substrates with different metallization layers*

3.2.1. *Microstructure of sintered Ag*

Fig. 10 shows the SEM images of the sintered Ag for the ENF specimens with different metallization layers sintered under different temperatures. A clear particle growth and densification tendency is found with the increase of the sintering temperature for each kind of specimen. When sintered under 240 °C for 60 min, most of the Ag particles are isolated and only a few of sintering necks are formed. However, the microstructure of the sintered Ag becomes coarsening and the necks are grown up after sintered under 300 °C for 60 min. The variations of the Ag particle size and porosity of sintered Ag with the sintering temperature are shown in Fig. 11. The results show that the Ag particle size increases with the increase of the sintering temperature, while the porosity decreases with the increase of the sintering temperature. Moreover, the Ag particle sizes and porosity of the sintered Ag for different specimens sintered under the same temperature are without remarkable difference, which indicates that the microstructure characteristic parameters of the sintered Ag is independent with the metallization layers.

The particle growth mechanism can be explained by the diffusion-related Ostwald ripening law and the growth process obeys a power-law model which is written as [46]:

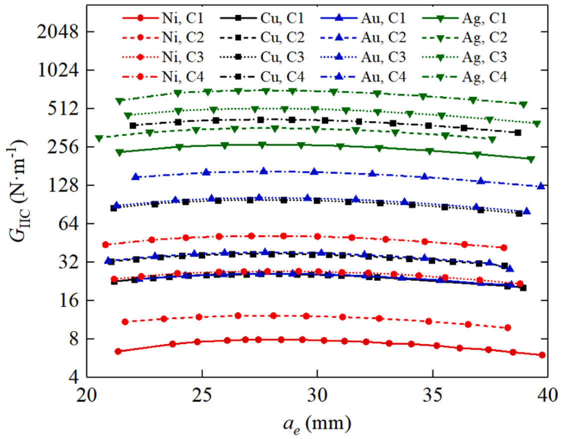

Fig. 4. Representative *R*-curves for different metallized specimens sintered under various temperatures.

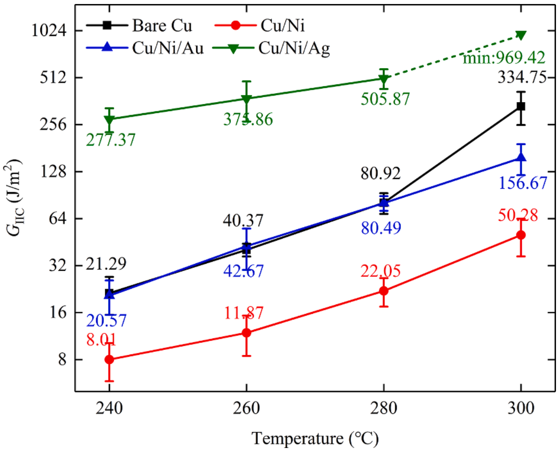

Fig. 5. Average G_{IIC} of the sintered Ag joints on Cu substrates with different metallization layers under various sintering temperatures.

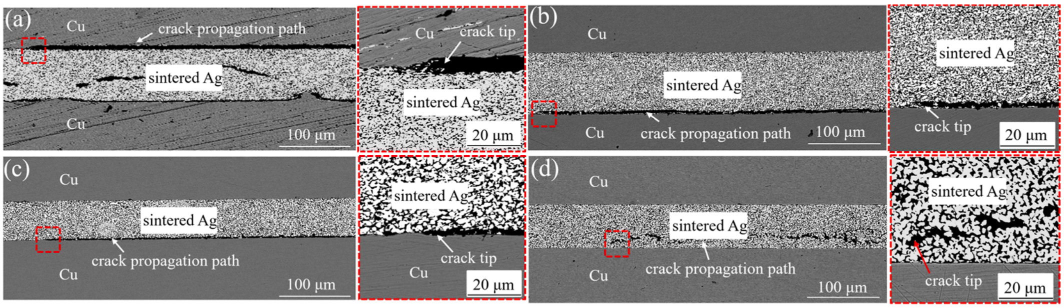

Fig. 6. Fracture morphologies of the ENF specimens with bare Cu substrates sintered at various temperatures. (a) 240 °C; (b) 260 °C; (c) 280 °C; (d) 300 °C.

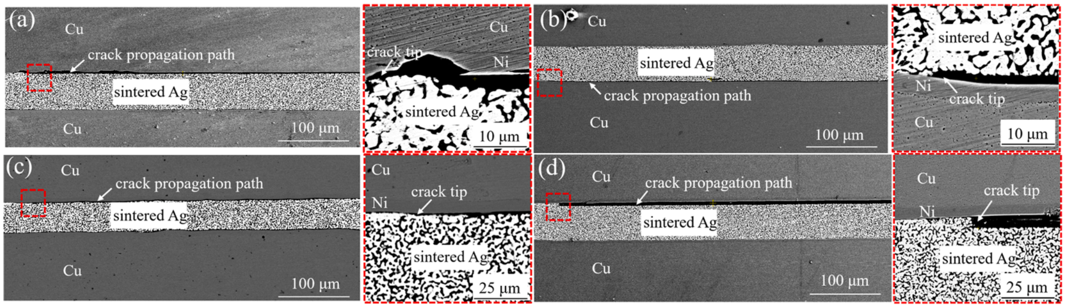

Fig. 7. Fracture morphologies of the ENF specimens with plated Ni layers sintered at various temperatures. (a) 240 °C; (b) 260 °C; (c) 280 °C; (d) 300 °C.

$$D^3 - D_0^3 = K_0 exp(-\frac{E_a}{QT}) \cdot t \tag{10}$$

where D is the particle diameter, D_0 is the initial particle diameter, K_0 is a constant, E_a is the activation energy, Q is the gas constant, T is the absolute temperature and t is the time. Similarly, the densification process of sintered Ag is also related to the diffusion mechanism of Ag particles and can be expressed by the following equation [47]:

$$ln(\frac{\theta}{\theta_0}) = C_0 exp(-\frac{E_a}{QT}) \cdot t^{1/3} \tag{11}$$

where θ is the porosity, θ_0 is the initial porosity, and C_0 is a constant. According to Eq. (5) and Eq. (6), it can be concluded that an elevated sintering temperature can enhance the growth rate of the Ag particle and the densification rate of the sintered Ag. The reason

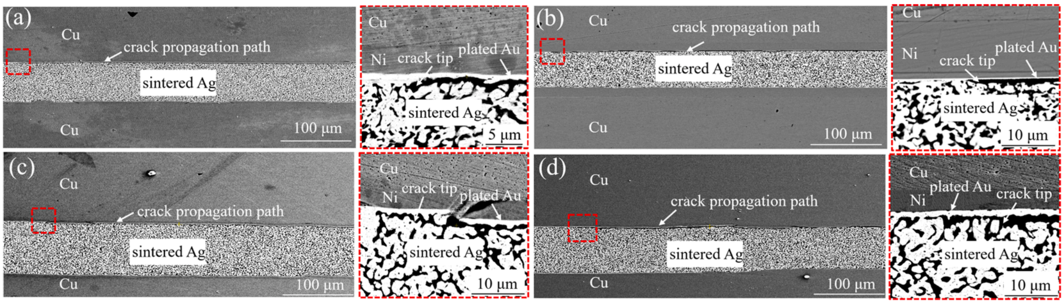

Fig. 8. Fracture morphologies of the ENF specimens with plated Ni/Au layers sintered at various temperatures. (a) 240 °C; (b) 260 °C; (c) 280 °C; (d) 300 °C.

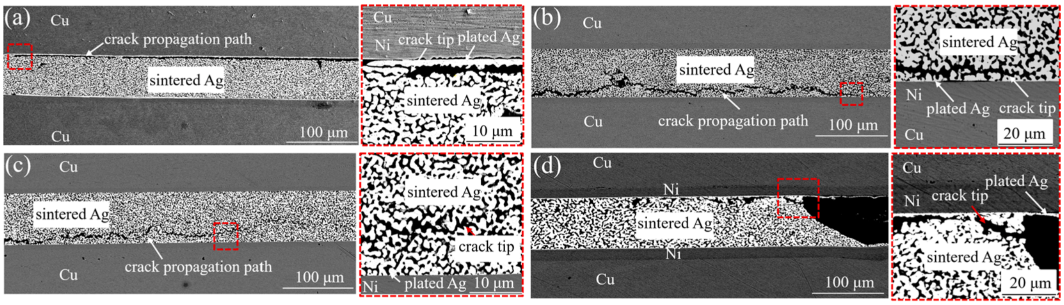

Fig. 9. Fracture morphologies of the ENF specimens with plated Ni/Ag layers sintered at various temperatures. (a) 240 °C; (b) 260 °C; (c) 280 °C; (d) 300 °C.

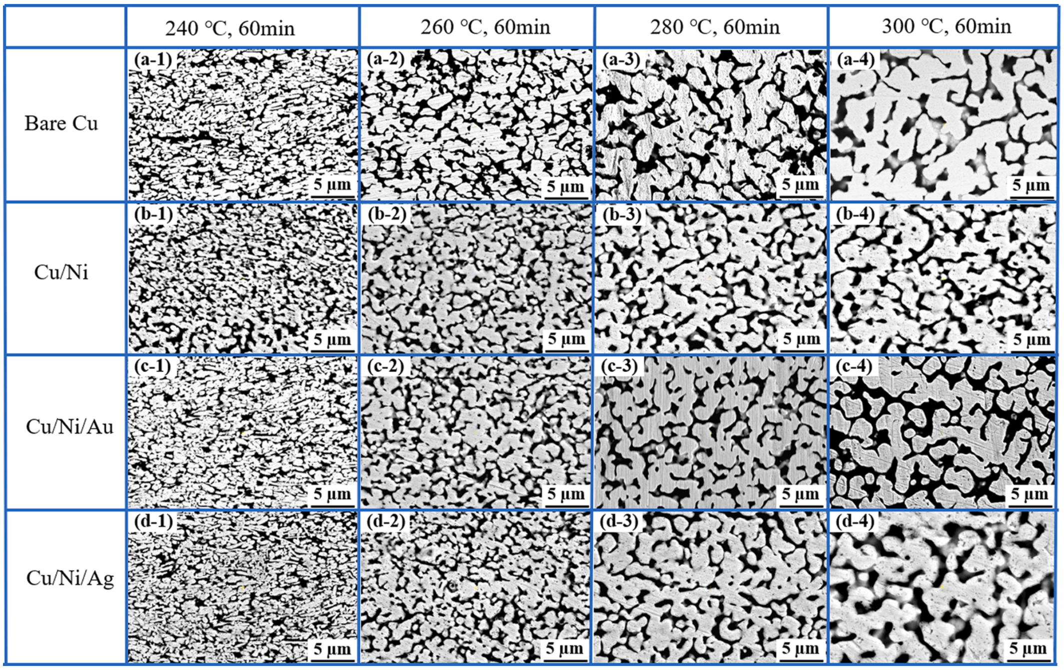

Fig. 10. SEM images of sintered Ag for the ENF specimens with different metallization layers sintered under different temperatures.

for that is a high sintering temperature improves the diffusion rate of the Ag atoms. Comparing Fig. 5 with Fig. 11, it is deduced that the growth of Ag particle size and decrease of porosity are related to the heightening of G_{IIC}. In other words, the particle size growth and densification of the sintered Ag layer are two main reasons that lead to the increase of G_{IIC} with the sintering temperature. However,

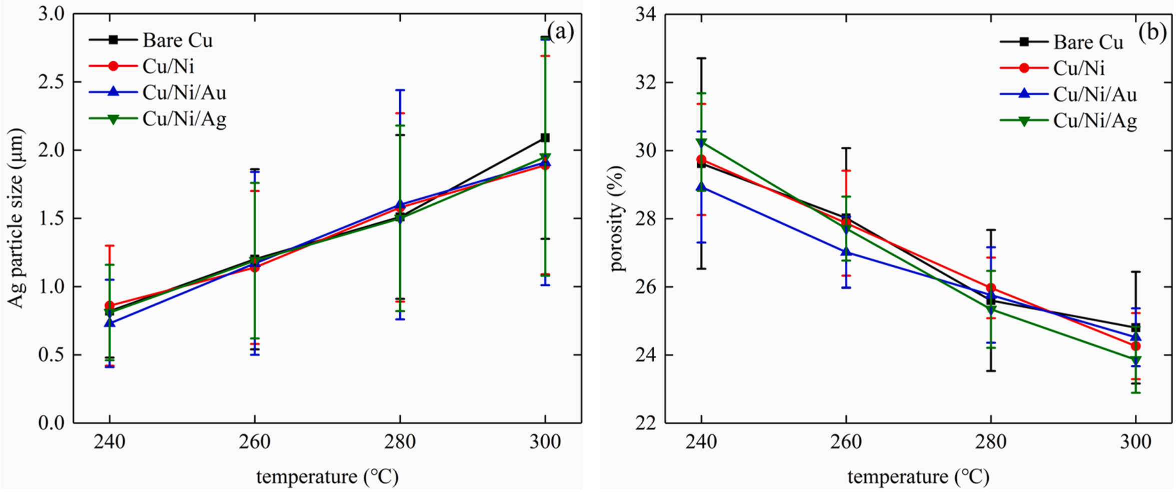

Fig. 11. Variations of microstructure characteristic parameters of sintered Ag for the ENF specimens with different metallization layers sintered under different temperatures. (a) The average Ag particle size; (b) the average of porosity.

the results also show that the difference of G_{IIC} for specimens with different metallization layers are barely related to the particle size and porosity of sintered Ag, due to these two items are almost the same for the specimens with different metallization layers even under the same sintering process.

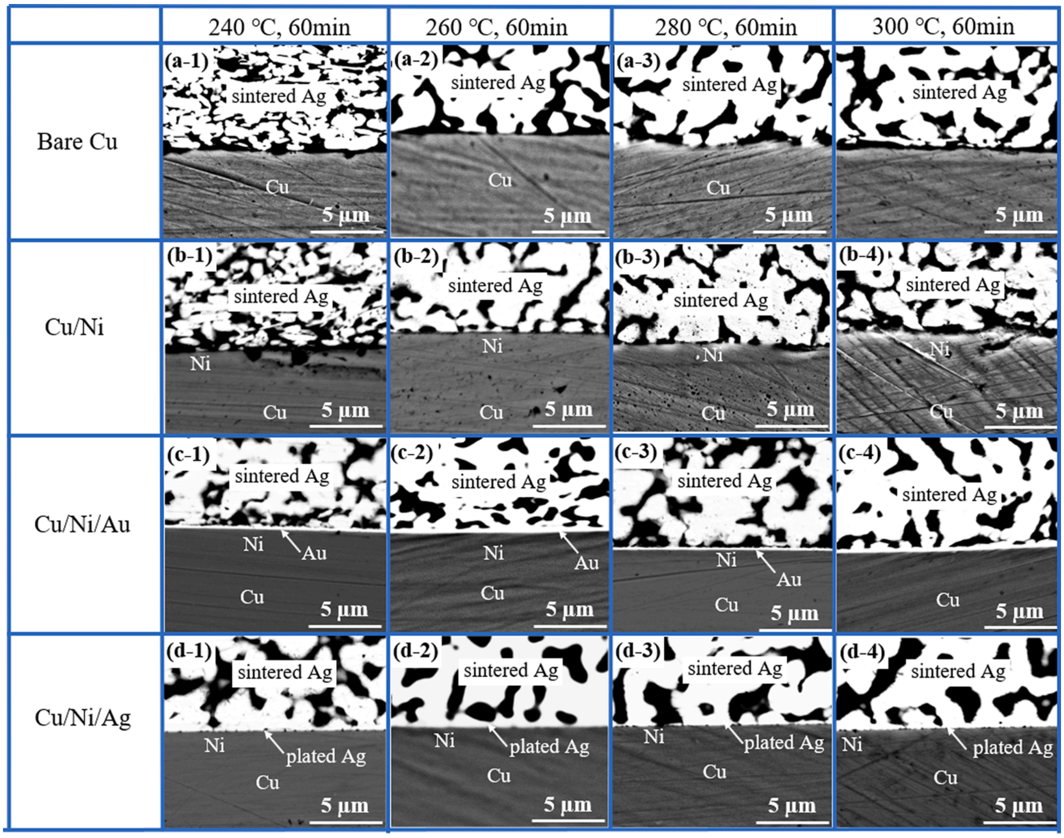

Fig. 12. SEM images of sintered Ag/substrate interface for the ENF specimens with different metallization layers sintered under various temperatures.

3.2.2. Microstructure of sintered Ag/substrate interface

Fig. 12 shows the typical SEM images of the sintered Ag/substrate interface for the ENF specimens with different metallization layers sintered under various temperatures. The results show that sintered Ag are bonded with the metallization layers well, however, the microstructures at the bonding interface are with obvious difference. To qualitatively characterize the interface connection quality, the interface connection ratios for each type of specimens sintered under various temperatures are calculated based on Eq. (9), and the results are shown in Fig. 13. All the interface connection ratio values increase with increasing sintering temperatures for all the specimens. The average value for Ni-plated specimens gradually increases from 24.6% to 28.4% with the sintering temperature increasing from 240 °C to 300 °C, which is lower than other kinds of specimens. For the Ni/Au-plated specimens, the interface connection ratio value increases from 28.7% to 33.7% in the same temperature variation range. As for the bare Cu specimens, when sintered under 240 °C, the average connection ratio value is 27.6%, which is a little lower than the Ni/Au-plated specimens. However, it increases to 39.7% when sintered under 300 °C, which is much higher than the Ni/Au-plated specimens. For all the ENF samples, the Ni/Ag-plated specimens show the highest interface connection ratio values, which increase from 50.4% to 65.7% with the increasing temperature from 240 °C to 300 °C.

The interface contact angles of the Ag particles and the metallization layer for the specimens sintered under various temperatures are also calculated and the distribution fractions of the calculated contact angle are shown in Fig. 14. For the Ni/Ag plated specimens, most of the contact angles are less than 90° and the fraction of the acute angle increases gradually with the increase of sintering temperature. However, for the other three kinds of specimens, most of the contact angles are obtuse angles.

Fig. 15 shows the variations of the average contact angles for different kinds of specimens with varied sintering temperature. All the average contact angles for different kinds of specimens decrease with the increase of sintering temperature. The average contact angles for the bare Cu and Ni-plated specimens are very close, while the average contact angle of the Au-plated specimens is a little lower than that of Cu and Ni-plated specimens. All the average contact angles for these three kinds of specimens are higher than 100°. However, for the Ag-plated specimens, the average contact angles are much lower than the others. For the Ni/Ag plated specimens, the average interface contact angle is 90.6° when sintered under 240 °C for 60 min, however, it decreases to 69.5° when sintered under 300 °C for 60 min.

4. Discussion

4.1. Effect of interfacial microstructure parameters on G_{IIC}

Fig. 16 shows the variation of average shearing fracture toughness G_{IIC} of different metallization layer-sintered Ag joints with their interface connection ratio and interface contact angles. An obvious correlation between G_{IIC} and the interface microstructure parameters can be obtained. It is seen that the average G_{IIC} increases with the augment of interface connection ratio and the decrease of interface contact angle. For the Ni-plated specimens, due to their lowest interface connection ratio and highest interface contact angles, the value of average G_{IIC} is the lowest compared with the other three kinds of specimens when sintered under the same sintering condition. On the contrary, the Ni/Ag-plated specimens possess the highest interface connection ratio and lowest interface contact angles, the average G_{IIC} is also the highest.

It is not difficult to understand the influencing mechanism of the interface connection ratio on the G_{IIC} of sintered Ag joints. A higher interface connection ratio will increase the actual cracking area during the crack propagation process. Hence, larger crack driving force is needed when the crack propagates along the interface of sintered Ag and metallization layers, which will increase the actual tested G_{IIC} correspondingly [48]. As to the effect of interface contact angle on G_{IIC}, a lower contact angle can significantly reduce

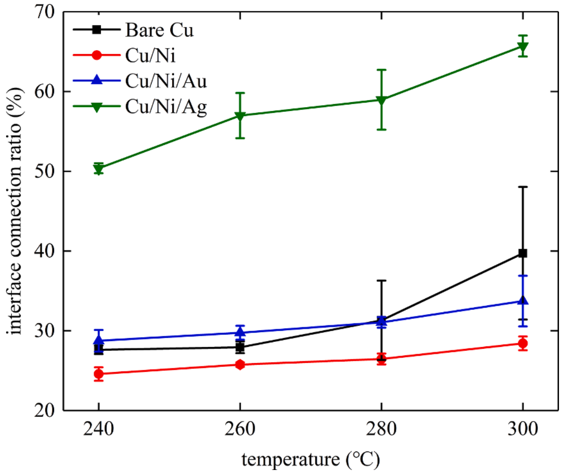

Fig. 13. Variations of the average interface connection ratio for the ENF specimens with different metallization layers sintered under various temperatures.

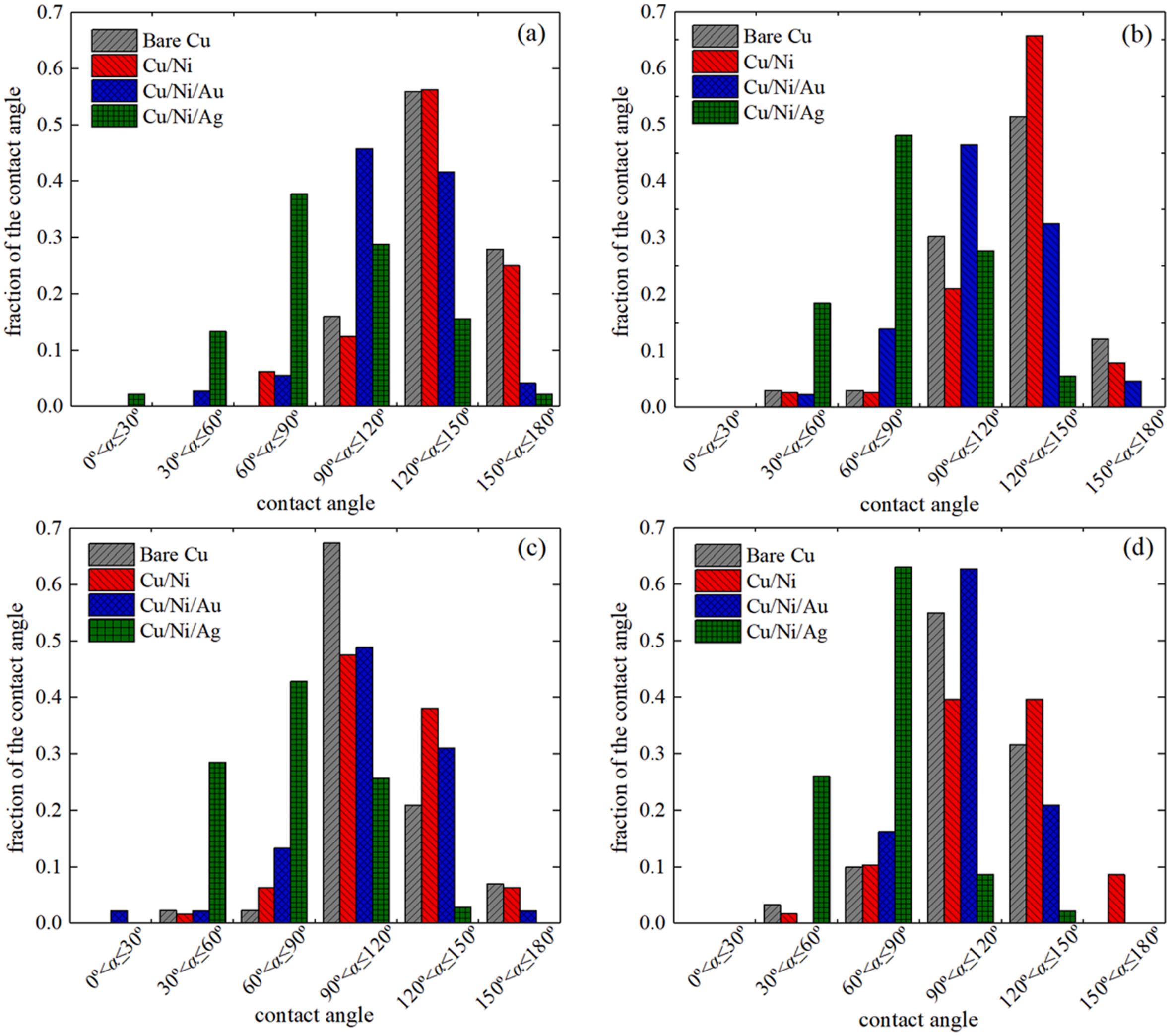

Fig. 14. Distribution of the interface contact angle for the specimens with different metallization layers sintered under various temperatures. (a) 240 °C for 60 min; (b) 260 °C for 60 min; (c) 280 °C for 60 min; (d) 280 °C for 60 min.

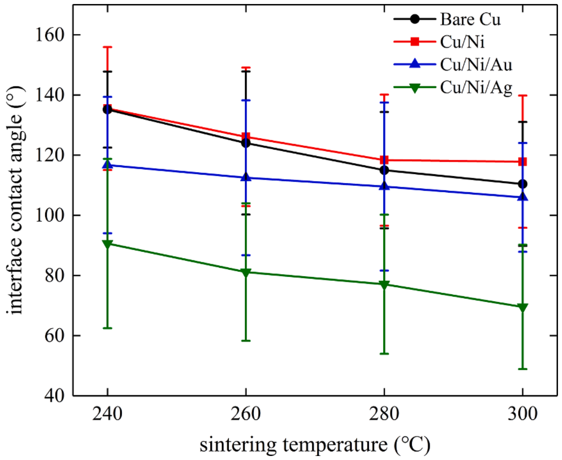

Fig. 15. Variations of the average interface contact angles with sintering temperature.

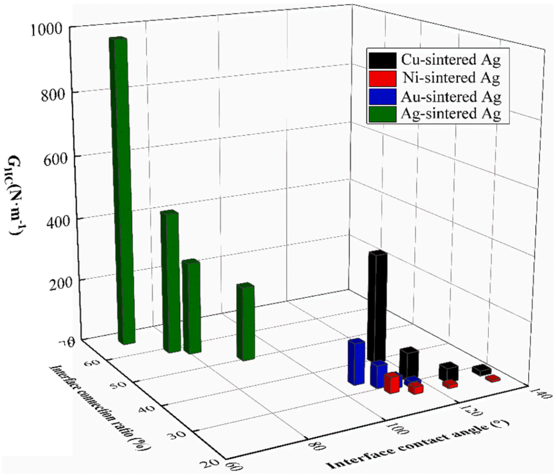

Fig. 16. Relationship between the interfacial microstructure parameters and average G_{IIC} of different metallization layer-sintered Ag joints.

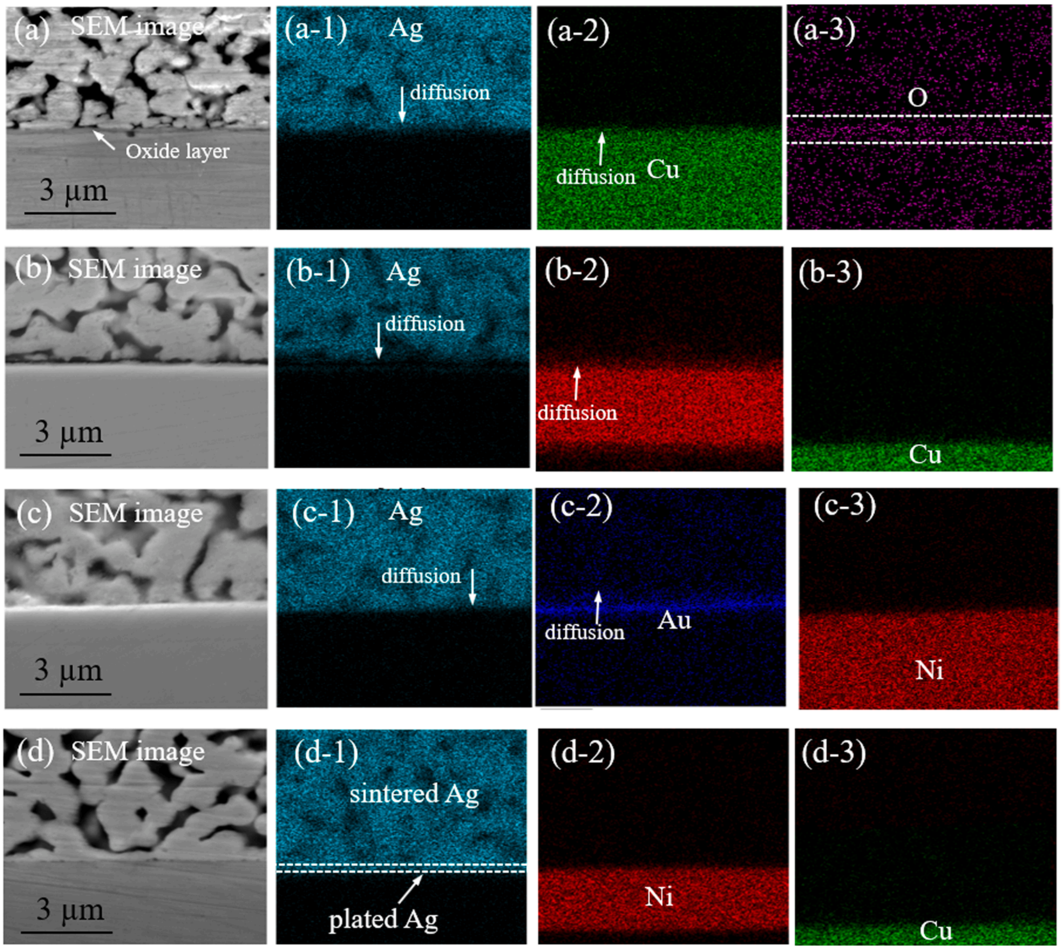

Fig. 17. Typical EDS mapping of the interfaces between sintered Ag and different metallization layers sintered under 300 °C. (a)-(a-3) SEM image and EDS mapping of sintered Ag/Cu interface; (b)-(b-3) SEM image and EDS mapping of sintered Ag/Ni interface; (c)-(c-3) SEM image and EDS mapping of sintered Ag/Au interface; (d)-(d-3) SEM image and EDS mapping of sintered Ag/Ag interface.

the stress singularity at the contact interface of sintered Ag and metallization layers, which will decrease the stress concentration distinctly when the specimens under shearing condition. With the increase of interface contact angles, more “V” shape notches are formed at the interface of sintered Ag and the metallization layers, which means many micro crack-tips are precast at the connection interface. Due to the stress concentration near the “V” shape notches, the crack forms easily along the interface between sintered Ag and the metallization layers under this condition, which will decrease the tested G_{IIC} correspondingly.

4.2. *Interface diffusion in the ENF specimens with different metallization layers*

To further confirm the mechanism of the sintered Ag bonded with different metallization layers, the interfacial element distributions are analyzed by the EDS. Fig. 16 shows the typical EDS mapping of the interfaces between sintered Ag and different metallization layers sintered under 300 °C. Clear inter-diffusion behaviors are observed at the sintered Ag/Cu, sintered Ag/Ni, and sintered Ag/Au interfaces. Though the inter-diffusion phenomenon can be hardly observed according to the EDS mapping, the sintered Ag and plated-Ag layers are connected very well which indicate reliable Ag-Ag bonding are formed. For the specimens with bare Cu substrate, a layer rich in oxygen element is formed between the sintered Ag/Cu interface, as shown in Fig. 17(a), which indicate that the surface of the Cu substrate is oxidated during the sintering process.

To quantificationally determine the interface reaction between the sintered Ag and metallization layers, the EDS line scan analysis is employed to characterize the interface inter-diffusion thickness for different specimens sintered from 240 °C to 300 °C, as shown in Fig. 18. The inter-diffusion thickness is defined as the distance between the two points where Ag and the metallization element on the opposite side possesses an atom percent of 10%, respectively [49]. The inter-diffusion thicknesses of the Ag/Cu, Ag/Ni and Ag/Au interface all increase with the increase of sintering temperature. It has been proved by many reports [42,50–51] that the fundamental mechanism of sintering and surface chemical reaction of sintered Ag joint with metallized substrates is based on atom diffusion. The atom diffusion rate can be expressed by the following equation [52]:

$$D = D_0 exp(-\frac{E_a}{QT}) \tag{12}$$

where D_0 is a pre-exponential factor related to atomic vibration frequency and jump distance. It can be concluded that the increase of diffusion thickness with increasing sintering temperature is due to the enhancement of the atom inter-diffusion rate by improvement of sintering temperature.

However, according to Fig. 18, the diffusion thickness at the interface between sintered Ag and different metallization layers under the same sintering temperature are obviously different. For the Ag/Cu interface, the diffusion thickness increases from 0.628 μm to 0.669 μm when the sintering temperature changes from 240 °C to 300 °C, while it increases from 0.574 μm to 0.608 μm for the Ag/Ni interface. For the Ag/Au interface, the diffusion thickness increases from 0.914 μm to 1.174 μm. The increasing rate and inter-diffusion thicknesses of the Ag/Au interfaces are much higher than that of the Ag/Ni and Ag/Cu interfaces, similar results are also reported by Lu et al. [53]. The reason for that is Au and Ag can be completely mixed in a solid solution rather than staying separation with minimum solubility of one in another, like the Au/Cu and Ag/Ni couples [53–54]. Though the EDS line scan analysis shown in Fig. 18 can hardly precisely determine the sintered Ag/plated-Ag inter-diffusion thickness, it is confirmed that the Ag-Ag inter-diffusion rate are higher than Ag-Au, Ag-Cu and Ag-Ni couples due to that diffusion barrier of Ag on Ag substrate shows a lowest value compared with that of Au, Ni and Cu substrates [55]. This indicates that the Ag atoms are easier to diffuse on an Ag-plated substrate than the other substates. Hence, the different inter-diffusion rates may be the reason leading to the discrepancy of interface connection ratio and contact angle between different metallized specimens despite the same sintering process.

To explain the effect of the inter-diffusion behaviors on the shearing fracture toughness G_{IIC} of the sintered Ag joints more clearly, the relationship between the inter-diffusion thicknesses of Cu-, Ni-, and Au-sintered Ag bonded joints and their average G_{IIC} values are summarized in Fig. 19. For each kind of metallization layer-sintered Ag joint, the G_{IIC} all increases with the increase of the inter-diffusion thickness. As mentioned above, the bonding mechanism of the sintered Ag and metallization layer are based on the atom diffusion. At the initial state of atom diffusion, a thicker inter-diffusion thickness represents more atomic bonds will be formed at the interface of sintered Ag and metallization layers. Therefore, the interface connection ratio and the shearing fracture toughness will increase correspondingly. However, for different metallization layer-sintered Ag joints, the values of G_{IIC} are quite different even at the same inter-diffusion thickness. This is related to the differences in the inter-diffusion rate for different inter-diffusion couples.

4.3. *Cu oxidation at the sintered Ag/Cu interface*

According to Fig. 17 (a-3) and Fig. 18 (a), there exists a layer of oxygen elements at the interface of Ag/Cu interface, especially when sintered in 300 °C, the thickness of the oxidation layer is much higher than the specimen sintered under 240–280 °C. To determine the contents of the oxidation layer, quantitative element point analysis along the Ag/Cu interface is performed, as shown in Fig. 20. The analysis results for different points are show in Table 1. It is seen that the atomic percent of oxygen of spectrum 2, 5, 8, and 11 is much higher than that of the other spectrums. This result is consistent with the observation in Fig. 17 and Fig. 18. Moreover, the ratios of At.% Cu and At.% O in these four spectrums are all approximate to 2:1, which indicates that the main composition in the oxidation layer is Cu_2O. It is known that the mismatch of lattice constants between Ag/Cu_2O is lower than that of Ag/Cu (Ag: 0.4086 nm, Cu_2O: 0.4260 nm, Cu: 0.3615 nm) [21]. A lower mismatch in lattice constants can reduce the lattice strain and interfacial energy, which is better for the chemical bond formation at the Ag/Cu and Ag/Cu_2O interfaces [21,55]. This may be the reason for the

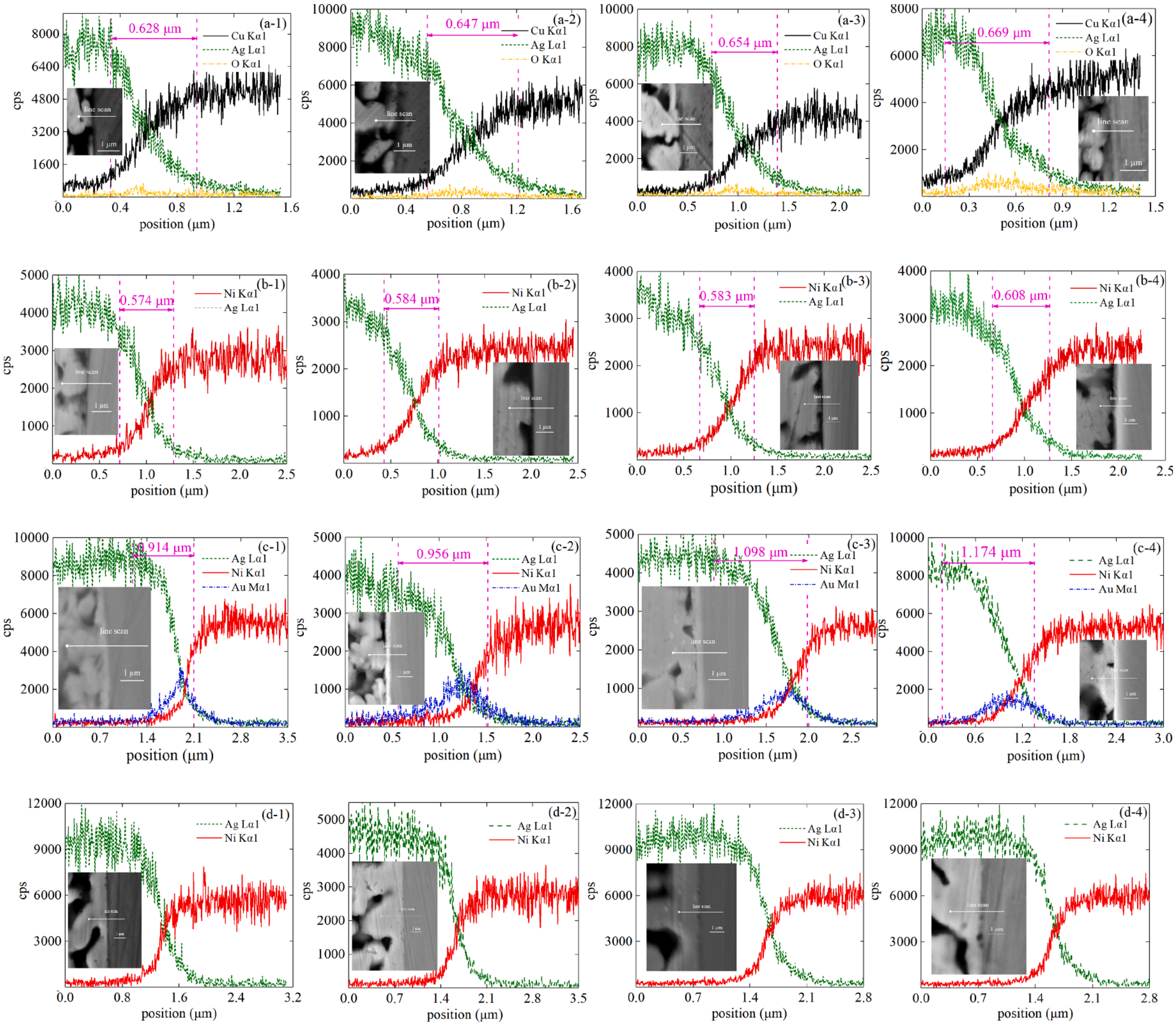

Fig. 18. Typical EDS line scan analysis of the interfaces between sintered Ag and different metallization layers sintered under different temperatures. (a) EDS line scan of sintered Ag/Cu interface; (b) EDS line scan of sintered Ag/Ni interface; (c) EDS line scan of sintered Ag/Au interface; (d) EDS line scan of sintered Ag/Ag interface.

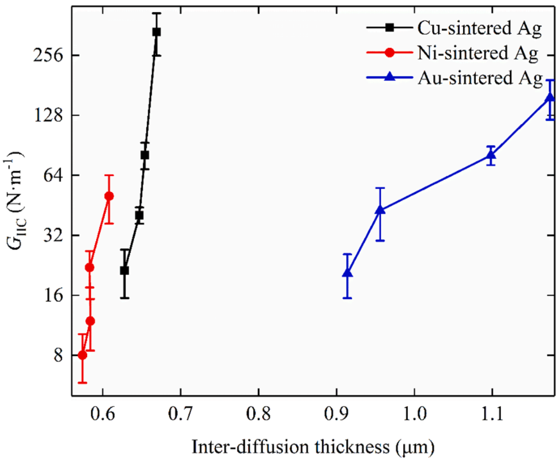

Fig. 19. Relationship between the inter-diffusion thicknesses of different metallization layer-sintered Ag joints and their average G_{IIC} values.

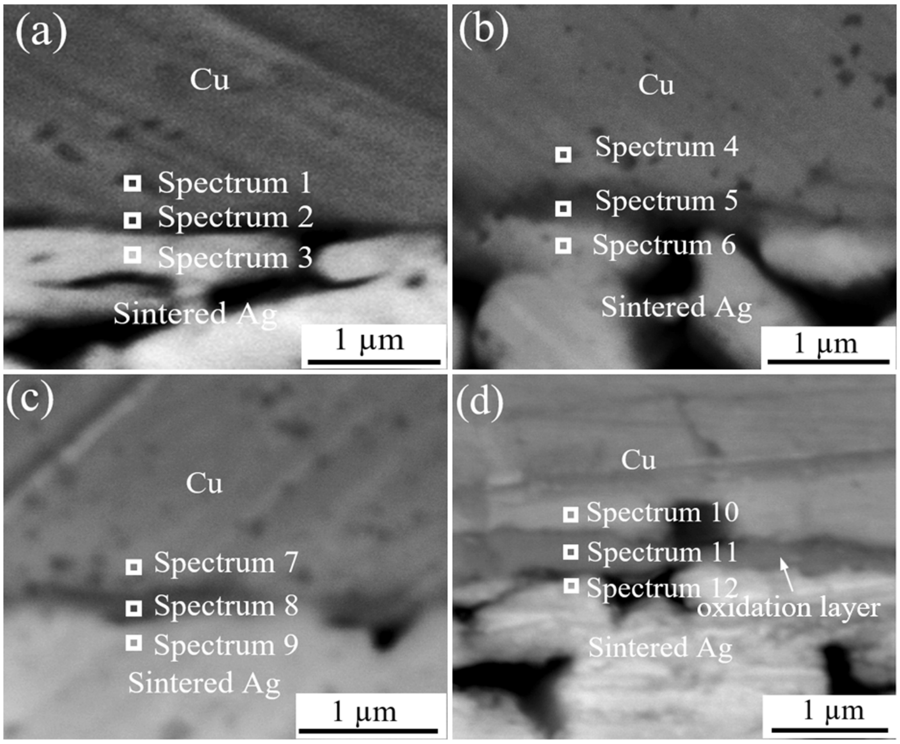

Fig. 20. EDS quantitative analysis points at the interface of sintered Ag and Cu. (a) sintered at 240 °C for 60 min; (b) sintered at 260 °C for 60 min; (c) sintered at 280 °C for 60 min; (b) sintered at 300 °C for 60 min.

Table 1
Element quantitative analysis results at different points.

Point	Wt.%			At.%		
	Ag L	Cu K	O K	Ag L	Cu K	O K
1	18.78	80.06	1.15	11.56	83.65	4.78
2	68.62	27.86	3.52	49.13	33.86	17.00
3	88.03	10.48	1.50	75.95	15.34	8.71
4	7.67	91.41	0.93	4.53	91.77	3.69
5	32.86	60.43	6.71	18.19	56.78	25.03
6	74.75	20.26	4.99	52.35	24.08	23.56
7	1.19	98.36	0.45	0.70	97.54	1.77
8	24.26	67.34	8.41	12.42	58.55	29.03
9	92.04	6.62	1.34	81.95	10.01	8.05
10	12.62	85.63	1.75	7.44	85.62	6.95
11	34.73	57.31	7.96	18.71	52.40	28.89
12	82.09	14.34	3.58	62.88	18.64	18.48

interfacial connection ratio and tested shearing fracture toughness of bare Cu specimens close to that of Ni/Au plated specimens with the inter-diffusion rate of Ag/Cu couples are much lower than Ag/Cu couples when sintered in 240–280 °C. In addition, with the rapid increase of the denser oxidation layer, the values of the G_{IIC} for the bare Cu specimens are further increased, which lead them much higher than that of those specimens metallized by Ag/Au layers.

5. Conclusions

In this paper, the effect of different surface finish metallization layers on the shearing fracture toughness of sintered silver joints under different sintering temperatures is studied and the main conclusions are drawn as follows:

1. The shearing fracture toughness of sintered Ag joint increases with the increasing of sintering temperature when sintered from 240 °C to 300 °C, regardless of metallization layer types. Under the same sintering process, the sintered Ag/Ag joint exhibits the highest average G_{IIC} value while the sintered Ag/Ni joint exhibits the lowest. The average G_{IIC} value of the Ag/Cu joint is a little lower than

that of Ag/Au joint when sintered from 240 °C to 280 °C. However, the G_{IIC} value of the Ag/Cu joint changes much higher than that of Ag/Au joint when sintered under 300 °C.
2. For the Ag/Ni joint and Ag/Au joint, the cracks all prone to propagate along the interface of Ag/Ni and Ag/Au when the sintering temperature varies from 240 °C to 300 °C. However, the crack propagation path changes from fracture along the interface (interface cracking) to fracture in the interior of sintered Ag layer (cohesive cracking) for the Ag/Cu and Ag/Ag joints with the sintering temperature increased from 240 °C to 300 °C.
3. The Ag particle size and porosity of sintered Ag are not the dominant factors affecting the discrepancies of shearing fracture toughness, G_{IIC}, among different kinds of metallized specimens, while the interface connection ratio and the contact angle are proved to be two dominant reasons.
4. The Ag-plated specimens possess the highest interface connection ratio and lowest contact angle, which can effectively increase the actual cracking area and reduce the stress concentration at the interface. These two main factors are the reasons that why the sintered Ag/Ag joint exhibits the highest average G_{IIC} value.
5. The possible reason for the difference of interface contact ratio and contact angle between different metallized specimens may be the effect of different inter-diffusion rate for different bi-metal couples. In addition, the formation of Cu_2O at the Ag/Cu interface can decrease the lattice strain and interfacial energy, which can also facilitate the increase of the contact interconnection ratio and tested G_{IIC} values.

This study shows a novel insight on deep understanding of the metallization layer effect on the shearing fracture toughness of sintered silver bonded joints. This investigation could also inspire the future work on improving the mechanical reliability of sintered silver by selecting suitable metallization layers.

CRediT authorship contribution statement

Shuai Zhao: Writing – original draft, Data curation, Formal analysis, Investigation, Methodology, Visualization. **Yanwei Dai:** Writing – review & editing, Supervision, Project administration, Methodology, Funding acquisition, Conceptualization. **Fei Qin:** Investigation, Resources, Supervision, Writing – review & editing. **Yanning Li:** Writing – review & editing. **Tong An:** Writing – review & editing. **Yanpeng Gong:** Writing – review & editing.

Declaration of Competing Interest

The authors declare that they have no known competing financial interests or personal relationships that could have appeared to influence the work reported in this paper.

Acknowledgment

The authors acknowledge the support from the National Natural Science Foundation of China (11902009), the Beijing Municipal Natural Science Foundation (2204074), and the Scientific Research Foundation of Beijing Municipal Commission of Education (KM202010005034).

References

[1] Yan J. A review of sintering-bonding technology using Ag nanoparticles for electronic packaging. Nanomaterials 2021;11(4):927.
[2] Jakubowska M, Jarosz M, Kiełbasinski K, Młożniak A. New conductive thick-film paste based on silver nanopowder for high power and high temperature applications. Microelectron Reliab 2011;51(7):1235–40.
[3] Chen G, Yu L, Mei Y-H, Li X, Chen Xu, Lu G-Q. Reliability comparison between SAC305 joint and sintered nanosilver joint at high temperatures for power electronic packaging. J Mater Process Tech 2014;214(9):1900–8.
[4] Hong WS, Kim MS, Oh C, Joo Y, Kim Y, Hong K-K. Pressureless silver sintering of silicon-carbide power modules for electric vehicles. JOM 2020;72(2):889–97.
[5] Siow KS, Chua ST, Beake BD, Zuruzi AS. Influence of sintering environment on silver sintered on copper substrate. J Mater Sci: Mater Electron 2019;30:6212–23.
[6] Mei Y-H, Cao Y, Chen G, Li X, Lu G-Q, Chen Xu. Characterization and reliability of sintered nanosilver joints by a rapid current-assisted method for power electronics packaging. IEEE T Device Mat Re 2014;14(1):262–7.
[7] Fu S, Mei YH, Ning P, Lu GQ. Parametric study on pressureless sintering of nanosilver paste to bond large-area (≥100 mm2) power chips at low temperature for electronic packaging. J Electron Mater 2015;44(10):3973–84.
[8] Yao Y, Gong He. Damage and viscoplastic behavior of sintered nano-silver joints under shear loading. Eng Fract Mech 2019;222:106741. https://doi.org/10.1016/j.engfracmech.2019.106741.
[9] Chen C, Nagao S, Zhang H, Jiu J, Sugahara T, Suganuma K, et al. Mechanical deformation of sintered porous Ag die attach at high temperature and its size effect for wide-band gap power device design. J Electron Mater 2017;46:1576–86.
[10] Chen C, Choe C, Zhang Z, Kim D, Suganuma K. Low-stress design of bonding structure and its thermal shock performance (-50 to 250℃) in SiC/DBC power die-attached modules. J Mater Sci: Mater Electron 2018;29:14335–46.
[11] Kim D, Chen C, Pei C, Zhang Z, Nagao S, Suetake A, et al. Thermal shock reliability of a GaN die-attach module on DBA substrate with Ti/Ag metallization by using micro/submicro Ag sinter paste. Jpn J Appl Phys 2019;58:SBBD15.
[12] Chen C, Zhang Z, Kim D, Zhang B, Tanioku M, Ono T, et al. Interfacial oxidation protection and thermal-stable sinter Ag joining on bare Cu substrate by single-layer graphene coating. Appl Surf Sci 2019;497:143797. https://doi.org/10.1016/j.apsusc.2019.143797.
[13] Lee BS, Yoon JW. Die-attach for power devices using the Ag sintering process: interfacial microstructure and mechanical strength. Met Mater Int 2017;23(5):958–63.
[14] Yoon JW, Back JH, Jung SB. Effect of surface finish metallization on mechanical strength of Ag sintered joint. Microelectron Eng 2018;198:15–21.
[15] Chen C, Suganuma K, Iwashige T, Sugiura K, Tsuruta K. High-temperature reliability of sintered microporous Ag on electroplated Ag, Au, and sputtered Ag metallization substrates. J Mater Sci: Mater Electron 2018;29:1785–97.

[16] Chen C, Suganuma K. Ag sinter joining technology for different metal interface (Au, Ag, Ni, Cu, Al) in wide band gap power modules. ECS Trans 2019;92(7):147–53.
[17] Xu Q, Mei Y, Li X, Lu GQ. Correlation between interfacial microstructure and bonding strength of sintered nanosilver on ENIG and electroplated Ni/Au direct-bond-copper (DBC) substrates. J Alloys Compd 2016;675:317–24.
[18] Fan T, Zhang H, Shang P, Li C, Chen C, Wang J, et al. Effect of electroplated Au layer on bonding performance of Ag pastes. J Alloys Compd 2018;731:1280–7.
[19] Wang M, Mei Y, Li X, Burgos R, Boroyevich D, Lu G-Q. Pressureless silver sintering on nickel for power module packaging. IEEE Trans Power Electron 2019;34(8):7121–5.
[20] Wang M, Mei Y, Li X, Lu GQ. Die-attach on nickel substrate by pressureless sintering a trimodal silver paste. Mater Lett 2019;253:131–5.
[21] Du CJ, Li X, Mei YH, Lu GQ. An explanation of sintered silver bonding formation on bare copper substrate in air. Appl Surf Sci 2019;490:403–10.
[22] Du CJ, Li X, Mei YH, Lu GQ. Bonding performance of sintered nanosilver joints on bare copper substrates with different grain structures. J Mater Sci: Mater Electron 2019;30:12860–8.
[23] Zhang Z, Chen C, Liu G, Li C, Kurosaka S, Nagao S, et al. Enhancement of bonding strength in Ag sinter joining on Au surface finished substrate by increasing Au grain-size. Appl Surf Sci 2019;485:468–75.
[24] Chen C, Zhang Z, Wang Q, Zhang B, Gao Y, Sasamura T, et al. Robust bonding and thermal-stable Ag-Au joint on ENEPIG substrate by micro-scale sinter Ag joining in low temperature pressure-less. J Alloys Compd 2020;828:15397.
[25] Msolli S, Baazaoui A, Alexis J, Kim HS. Identification of damage and fracture modes in power electronic packaging from experimental micro-shear tests and finite element modeling. Eng Fract Mech 2018;188:470–92.
[26] Zhang H, Zhao Z, Zou G, Wang W, Liu L, Zhang G, et al. Failure analysis and reliability evaluation of silver-sintered die attachment for high-temperature applications. Microelectron Reliab 2019;94:46–55.
[27] Wang S, Kirchlechner C, Keer L, Dehm G, Yao Y. Interfacial fracture toughness of sintered hybrid silver interconnects. J Mater Sci: Mater Electron 2020;55:2891–904.
[28] Qin F, Zhao S, Liu L, Dai Y, An T, Chen P, et al. Thickness and metallization layer effect on interfacial and vertical cracking of sintered silver layer: A numerical investigation. Microelectron Reliab 2021;124:114290. https://doi.org/10.1016/j.microrel.2021.114290.
[29] Schön J, Nyman T, Blom A, Ansell H. Numerical and experimental investigation of a composite ENF-specimen. Eng Fract Mech 2000;65(4):405–33.
[30] Delbariani-Nejad A, Malakouti M, Farrokhabadi A. Reliability analysis of metal-composite adhesive joints under debonding modes I, II, and I/II using the results of experimental and FEM analyses. Fatigue Fract Eng M 2019;42:2644–62.
[31] Silva MAL, Morais JJL, de Moura MFSF, Lousada JL. Mode II wood fracture characterization using the ELS test. Eng Fract Mech 2007;74(14):2133–47.
[32] Yoshihara H. Mode II *R*-curve of wood measured by 4-ENF test. Eng Fract Mech 2004;71(13-14):2065–77.
[33] Azevedo JCS, Campilho RDSG, da Silva JFG, Faneco TMS, Lopes RM. Cohesive law estimation of adhesive joints in mode II condition. Theor Appl Fract Mech 2015;80:143–54.
[34] Arrese A, Carbajal N, Vargas G, Mujika F. A new method for determine mode II R-curve by the End-Notched Flexure test. Eng Fract Mech 2010;77:51–70.
[35] Zhao S, Dai Y, Qin F, Li Y, Liu L, Zan Z, et al. On mode II fracture toughness of sintered silver based on end-notch flexure (ENF) test considering various sintering parameters. Mater Sci Eng A 2021;823:141729. https://doi.org/10.1016/j.msea.2021.141729.
[36] Dai Y, Zan Z, Zhao S, Li Y, Qin F. Shearing fracture toughness enhancement for sintered silver with nickel coated multiwall carbon nanotubes additive. Eng Fract Mech 2022;260:108181. https://doi.org/10.1016/j.engfracmech.2021.108181.
[37] de Moura MFSF, de Morais AB. Equivalent crack based analyses of ENF and ELS tests. Eng Fract Mech 2008;75:2584–96.
[38] Arrese A, Carbajal N, Vargas G, Mujika F. A new method for determining mode II R-curve by the end-notched flexure test. Eng Fract Mech 2010;77:51–70.
[39] Ayatollahi MR, Ajdani A, Akhavan-Safar A, da Silva LFM. Effect of notch length and pre-crack size on mode II fracture energy of brittle adhesives. Eng Fract Mech 2019;212:123–35.
[40] de Moura MFSF, Oliveira JMQ, Morais JJL, Xavier J. Mixed-mode I/II wood fracture characterization using the mixed-mode bending test. Eng Fract Mech 2010;77(1):144–52.
[41] de Moura MFSF, Campilho RDSG, Conçalves JPM. Pure mode II fracture characterization of composite bonded joints. Int J Solids Struct 2009;46:1589–95.
[42] Roh MH, Nishikawa H, Tsutsumi S, Nishiwaki N, Ito K, Ishikawa K, et al. Effect of temperature and substrate on shear strength of the joints formed by sintering of micro-sized Ag particle paste without pressure. J Mater Sci: Mater Electron 2017;28(10):7292–301.
[43] Zhang H, Wang W, Bai H, Zou G, Liu L, Peng P, et al. Microstructural and mechanical evolution of silver sintering die attach for SiC power devices during high temperature applications. J Alloys Compd 2019;774:487–94.
[44] Zabihzadeh S, Van Petegem S, Holler M, Diaz A, Duarte LI, Swygenhoven HV. Deformation behavior nanoporous polycrystalline silver. Part I: microstructure and mechanical properties. Acta Mater 2017;131:467–74.
[45] da Silva LFM, de Magalhães FACRG, Chaves FJP, de Moura MFSF. Mode II fracture toughness of a brittle and ductile adhesive as a function of the adhesive thickness. J Adhesion 2010;86:891–905.
[46] Park SJ, Martin JM, Guo JF, Johnson JL, German RM. Grain growth behavior of tungsten heavy alloys based on the master sintering curve concept. Metall Mater Trans A Phys Metall Sci 2006;37:3337–46.
[47] Gómez SY, Hotza D. Predicting powder densification during sintering. J Eur Ceram Soc 2018;38:1736–41.
[48] Ashby MF. The mechanical properties of cellular solid. Metall Mater Trans A 1983;14A:1755–69.
[49] Zhao SY, Li X, Mei YH, Lu GQ. Study on high temperature bonding reliability of sintered nano-silver joint on bare copper plate. Microelectron Reliab 2015;55:2524–31.
[50] Paknejad SA, Dumas G, West G, Lewis G, Mannan SH. Microstructure evolution during 300℃ storage of sintered Ag nanoparticles on Ag and Au substrates. J Alloys Compd 2014;617:994–1001.
[51] Akada Y, Tatsumi H, Yamaguchi T, Hirose A, Morita T, Ide E. Interfacial bonding mechanism using silver metallo-organic nanoparticles to bulk metals and observation of sintering behavior. Mater Trans 2008;49(7):1537–45.
[52] Li XX, Yang C, Chen T, Fu ZQ, Li YY, Ivasishin OM, et al. Determination of atomic diffusion coefficient via isochronal spark plasma sintering. Scripta Mater 2018;151:47–52.
[53] G.Q. Lu, M. Wang, Y. Mei, X. Li, Advanced die-attach by metal-powder sintering: the science and practice. 10th International Conference on Integrated Power Electronics Systems (CIPS); Mar. 2018.
[54] Lin Y-C, Jean J-H. Constrained sintering of silver circuit paste. J Am Ceram Soc 2004;87(2):187–91.
[55] Zhang Z, Chen C, Yang Y, Zhang H, Kim D, Sugahara T, et al. Low-temperature and pressureless sinter joining of Cu with micro/submicron Ag particle paste in air. J Alloys Compd 2019;780:435–42.